Hindawi
Geofluids
Volume 2022, Article ID 7465919, 9 pages
https://doi.org/10.1155/2022/7465919

Research Article

Application of GPR Underground Pipeline Detection Technology in Urban Complex Geological Environments

Xiaoqiang Liang,[1,2] Da Hu,[1,2,3] Yongsuo Li,[1] Yunyi Zhang,[1,2] and Xian Yang[4]

[1]*Hunan Engineering Research Center of Structural Safety and Disaster Prevention for Urban Underground Infrastructure, Hunan City University, Yiyang 413000, China*
[2]*Key Laboratory of Metallogenic Prediction of Nonferrous Metals and Geological Environmental Monitoring, Ministry of Education, Central South University, Changsha 410083, China*
[3]*Hunan Provincial Key Laboratory of Key Technology on Hydropower Development, Power China Zhongnan Engineering Co. Ltd., Changsha 410014, China*
[4]*School of Resource, Environment and Safety Engineering, Hunan University of Science and Technology, Xiangtan, Hunan 411201, China*

Correspondence should be addressed to Da Hu; huda@hncu.edu.cn

Received 6 March 2022; Accepted 21 April 2022; Published 20 May 2022

Academic Editor: Zhongguang Sun

In the process of the continuous construction of underground pipelines, underground pipe network systems have become increasingly complex, which puts forward higher requirements for normal operation and maintenance. To address different kinds of complex conditions, this experiment in the present paper takes ground penetrating radar as the research basis and uses a self-correction and screening algorithm to innovatively detect underground pipelines. The results show that urban underground pipeline detection technology based on ground penetrating radar (GPR) can obtain a highly reliable number of pipelines and track predefined pipelines when detecting different numbers of verification pipelines. When detecting underground pipelines in different sections, the vertical and horizontal errors are no more than 0.199 m and 0.248 m, respectively, which means that the detection technology of urban underground pipelines based on GPR has high detection accuracy and can be performed on high-level detection tasks under various complex conditions. This research applies bottom detection radar to urban underground pipeline detection technology under complex conditions for the first time, innovatively uses the action mechanism of bottom detection radar, integrates its high precision and high efficiency into underground pipeline detection technology, and ensures the effectiveness of the detection work.

1. Introduction

The urban underground pipe network system is expanding and becoming increasingly complex, including underground pipelines in many fields, such as telecommunications, electric power, heat, water supply, and drainage. Because different units manage underground pipelines in different fields, the current information management system of urban underground pipelines is relatively disordered, exposing many problems, such as a lack of corresponding map information and incomplete line coordinate information [1]. In this case, it is urgent to reposition the urban underground pipeline and redraw the map, so optimizing the urban underground pipeline detection technology is the first priority. At present, the more common detection technologies are microgravity detection, tracing methods, electromagnetic induction methods, mechanical detection, etc. However, China has wide land coverage and high geological and geomorphic complexity [2–6], and such detection technologies have certain disadvantages, such as inaccurate positioning, low efficiency, and high cost, which make it difficult to successfully complete various detection tasks under complex conditions [7, 8]. The commonly used urban underground pipeline detection technology does not reasonably apply

ground penetrating radar. When performing the detection task under complex terrain conditions, it cannot accurately detect the obstacles affecting the construction operation, such as buried lines, which makes it difficult to control the construction time and project quality.

As an effective detection technology, ground penetrating radar is widely used in various fields with its intelligent and efficient electromagnetic pulse reflection technology, which can provide a large amount of high-resolution data and high-precision information for research work [9]. Nevertheless, GPR will show different detection accuracies in different application positions and states. In view of this, this subject experiment will deeply analyze urban underground pipeline detection technology based on GPR to provide strong technical support for the operation and maintenance of urban underground pipelines.

2. Detection Technology and Algorithm Design Based on GPR

2.1. Technical Principle of GPR. GPR is an electromagnetic pulse reflection method similar to reflection seismology. It can be used to realize effective detection of underground material distribution [10]. In the simple time-domain form of GPR, an electromagnetic pulse will be transmitted to the ground, and part of the energy will be reflected. Generally, the magnetic permeability is approximately $4\pi * 10^{-7}$ V·s/(A·m), and the dielectric constant and conductivity together determine the reflectivity of the rock boundary [11, 12]. In addition, in the GPR detection process, the antenna is usually placed flatly on the ground to meet the optimal grounding coupling state. Compared with setting the antenna in air, this method can significantly improve the characteristics of the antenna, and a high pulse rate can push the antenna forward to obtain a robust continuous detection effect. The principle of GPR is shown in Figure 1.

From Figure 1, it is shown that the detection technology based on GPR has strong noninvasive characteristics, which can provide the system with high-resolution data information and is able to summarize and analyze the above data. Finally, the radar image results with integrity and real time are displayed on the plotter. The maximum value of the wide pulse spectrum is often determined by the size of the target to be detected, and the dielectric coefficient is expressed as ε, usually with a value of approximately 9. The conductivity is expressed as σ [13].

Regarding the GPR image as a two-dimensional matrix containing multiple pixels, the clustering algorithm is needed to find the possible hyperbolic submatrix. First, the GPR image is preprocessed by clustering, and the transformation from the original image to the binary image is realized by inputting the adaptive threshold of the image [14, 15]. To identify hyperbolic features from the clustering algorithm, the related attributes representing hyperbolic features need to be extracted. In the GPR image, the detected hyperbolic branch must be displayed as a downward opening, and its general program is shown as follows:

$$\frac{(y-y_0)^2}{a^2} - \frac{(x-x_0)^2}{b^2} = 1, \text{with } y < y_0. \tag{1}$$

In Equation (1), (x_0, y_0) is the center of the hyperbola, a is the length of the semimajor axis, b is the length of the semiminor axis, x is the distance along the measuring direction, and y is positively correlated with the travel time of the wave. The first derivative form of the function shown in Equation (1) can be seen as follows:

$$\frac{dy}{dx} = -\frac{a}{b}\frac{x-x_0}{\sqrt{(x-x_0)^2+b^2}}. \tag{2}$$

The second derivative can be expressed as follows:

$$\frac{d^2y}{dx^2} = -\frac{ab}{\left((x-x_0)^2+b^2\right)^{3/2}}. \tag{3}$$

According to Equations (2) and (3), the shape of the curve derivative can be drawn and compared with the predefined hyperbola so that the predefined hyperbola is expressed as $y^2/25 - x^2/16 = 1$, and the similarity of the two curves in the normalized cross-correlation value can be obtained [16, 17].

2.2. Layout of GPR. In the detection process, the GPR device usually has to move along a scanning line that intersects with the underground pipeline. When it detects the intersection of the underground pipeline and the scanning line, the detection signal will change [18]. The scanning lines of GPR need to be reasonably arranged to ensure the detection efficiency and data quality to obtain a better detection effect of underground pipeline [19]. Figure 2 shows two common layouts in practice, i.e., the parallel line and zigzag.

The angle between any underground pipeline and scanning line in Figure 2 is θ_{bs}. Only when $\theta_{bs} > 60^\circ$ will the intersection be valid, and the signal there will change significantly. According to Figure 2, each pair of parallel dotted lines is spreading or parallel or Z-shaped scanning lines, and the cross column long strip is the underground pipeline.

Compared with the two layout methods, although the number of valid intersections of the parallel line layout is greater in the first layout, the effective range angle θ_r of the Z-shaped layout is larger in the second layout; thus, the second layout is more applicable. To further compare the advantages and disadvantages of the two layouts, quantitative analysis can be conducted. First, the same number of valid intersections is given with the lower limit of k. Then, the B values of the two layouts are set to 1. In the first parallel layout, Equation (4).

$$\frac{B}{kA} = \tan\left(\frac{\pi}{6}\right). \tag{4}$$

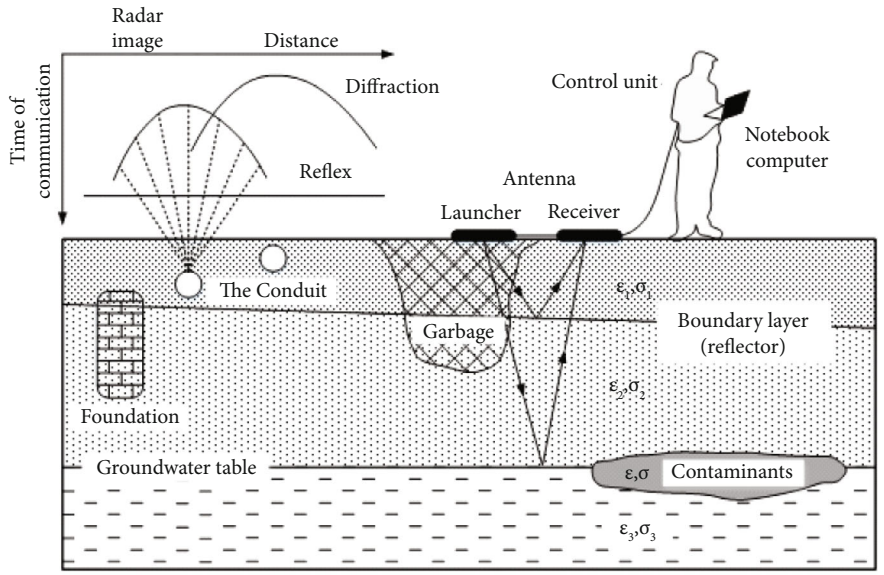

Figure 1: Configuration diagram of the ground-penetrating radar antenna.

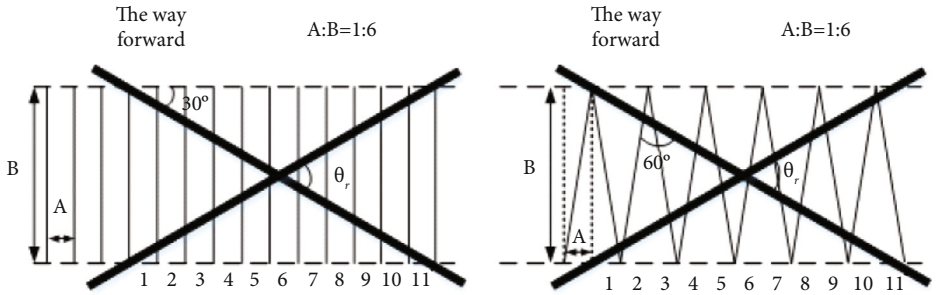

(a) Parallel line layout (b) Zigzag layout

Figure 2: Layout comparison of parallel lines and zigzags.

According to the above equation, Equation (5) can be deduced:

$$D = k\tan\left(\frac{\pi}{6}\right),$$
$$4 \le k \le 6 \Longrightarrow 2.3 \le D \le 3.5. \tag{5}$$

In the second Z-shaped layout, if the angle between the underground pipeline and the long-distance scanning line is θ, then Equation (6) can be obtained.

$$\frac{B}{\cos(\theta)\sin(\theta + \pi/6)} = \frac{2kA}{\sin(\pi/3)}. \tag{6}$$

Combining the above contents with Equations (4) to (6) leads to the following:

$$\sqrt{3}D^2 - 2kD + \sqrt{3} - 2\sqrt{3}k = 0,$$
$$\Longrightarrow D = \frac{k + \sqrt{k^2 + 6k - 3}}{\sqrt{3}},$$
$$4 \le k \le 6 \Longrightarrow 5.82 \le D \le 8.26. \tag{7}$$

When the density is determined, the path cost of the unit forward direction can be calculated. If the path of the parallel line layout needs to be the shortest, then

$$A + B \le 2\sqrt{B^2 + \left(\frac{1}{2}A\right)^2} \Longrightarrow \frac{2}{3} \le \frac{B}{A}. \tag{8}$$

When k is not less than 6, then Equation (8) needs to be satisfied, resulting in a shorter path using the parallel line layout. However, then

$$pf = \frac{R(n)}{\theta_r}. \tag{9}$$

In Equation (9), pf represents the scanning path cost of any unit angle underground pipeline in the process of detection, $R(n)$ represents the path length of any scanning cycle when the density D reaches the minimum value, and $k \le n$ [20]. The curves of the two layouts under different k values can be obtained by combining the former formulas.

According to Figure 3, it can be seen that when the number of valid intersections and the B value of the two layouts is consistent, the scanning path of the Z-shaped layout is longer than that of the parallel layout.

2.3. Self-Correction and Screening Algorithm for Drawing Underground Pipelines. According to the above investigation, there is a certain intersection between the scanning line and the underground pipeline between two parallel lines. To locate this intersection, different indication alarms are needed. One case has a correct alarm; that is, the alarm is located at the intersection. The second case has a false alarm; that is, the location of the alarm is not at the intersection. The third case is without the alarm; that is, there is no alarm at the intersection [21, 22]. Any alarm point can be represented by a detection vector, as shown as follows:

$$\mathrm{DV} = <x, y, z, r, dx, dy, dz> . \tag{10}$$

In Equation (10), r represents the radius length of the underground pipeline, (x, y, z) represents the three-dimensional coordinates of the alarm point, and (dx, dy, dz) represents the direction of the underground pipeline. The structure of the underground pipeline can be expressed as $<\mathrm{len}, \vec{\mathrm{pos}}, \vec{\mathrm{dir}}, r, \mathrm{DVList}, \mathrm{DN}, \mathrm{MVP}, \mathrm{MDA}>$, where len is the length of the underground pipeline, $\vec{\mathrm{pos}}$ is the center point of the underground pipeline, $\vec{\mathrm{dir}}$ is the estimated direction of the underground pipeline, and DN is the number of detection vectors [23]. MVP and MDA represent the mean value of the position change from the detection vector to the fitting line and the mean value of its angle deviation, respectively, as shown in Figure 4.

In Figure 4, the long arrow of the solid line represents the scan line for detection, the two short dark gray filled bars represent detection vector DV, the long light gray filled bar represents the underground pipeline obtained by fitting, and the two dots represent the alarm points obtained during the detection. As shown in Figure 4, the detection vector is usually in unit length, so only the direction of the vector needs to be obtained. The length of the underground pipeline changes with the operation of the self-correction and screening underground pipeline drawing algorithm. Let any DVList include the n-term DV from DV_1 to DV_n, and let $|\vec{\mathrm{dir}}| = 1$, $\vec{dv}_i = (\mathrm{DV}_i.dx, \mathrm{DV}_i.dy, \mathrm{DV}_i.dz)$, $\vec{v}_i = (\mathrm{DV}_i.x, \mathrm{DV}_i.y, \mathrm{DV}_i.z)$; then, Equation (11) can be obtained.

$$\begin{aligned} \mathrm{DN} &= n, \\ \mathrm{MVP} &= \frac{1}{n}\sum_{i=1}^{n}\left\|\left(\vec{v}_i - \vec{\mathrm{pos}}\right) - \left[\left(\vec{v}_i - \vec{\mathrm{pos}}\right)\cdot\vec{\mathrm{dir}}\right]\cdot\vec{\mathrm{dir}}\right\|_2, \\ \mathrm{MDA} &= \frac{1}{n}\sum_{i=1}^{n}\arccos\left(\frac{\left|\vec{\mathrm{dir}}\cdot\vec{dv}_i\right|}{\left|\vec{\mathrm{dir}}\right|\cdot\left|\vec{dv}_i\right|}\right). \end{aligned} \tag{11}$$

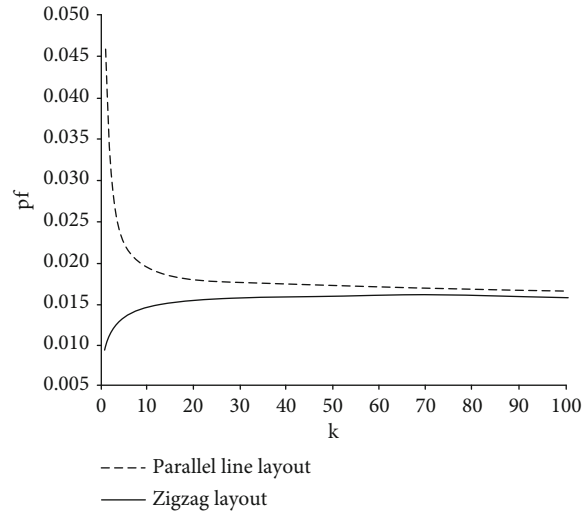

Figure 3: The pf curve of two layout modes under different k values.

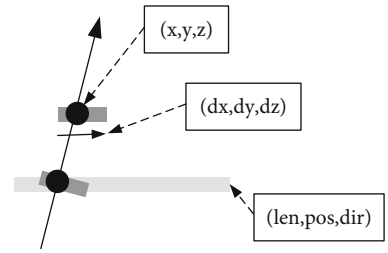

Figure 4: Data structure of the detection vector and underground pipeline.

There is a specific screening condition in Equation (11), that is, the boundary, which can be expressed as a combination of operations, as shown as follows [24]:

$$\begin{aligned} \mathrm{score} &= \frac{\mathrm{DN}}{N_0}\times\frac{P_0}{\mathrm{MVP}}\times\frac{A_0}{\mathrm{MDA}}, \\ \mathrm{boundary} &= (\mathrm{score} > \mathrm{threshold})?\mathrm{true} : \mathrm{false}. \end{aligned} \tag{12}$$

In addition, the boundary can also be expressed as a logical combination, as shown as follows:

$$\mathrm{boundary} = \mathrm{DN} > N_0 \wedge \mathrm{MVP} \le P_0 \wedge \mathrm{MDA} \le A_0. \tag{13}$$

A visual description of the self-correcting and filtering algorithm for underground pipeline drawing is shown in Figure 5.

Figure 5(a) shows the three situations in which alarm points are obtained in the detection process. They are an error DV, a correct DV, and a missing intersection. As shown in Figure 5(b), the underground pipeline drawing algorithm based on self-correction and screening is an iterative function. Whenever a scan line starts to be detected, the algorithm generates an update iteration. The binary relationship in the underground pipeline can be defined as follows:

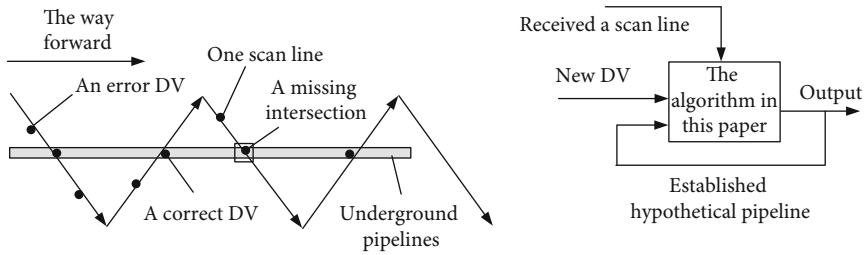

(a) Detection diagram (b) Trigger model

Figure 5: Visual schematic diagram of detection.

$$\begin{gathered}\text{pipel conflict pipe2} \equiv \\ \exists \mathrm{DV}_0 : \mathrm{DV}_0 \in \text{pipe1.DVList} \mathrm{UDV}_0 \hat{\mathrm{I}} \text{pipe2.DVList}\end{gathered}. \quad (14)$$

The drawing algorithm for the underground pipeline based on self-correction and filtering is mainly divided into three steps: modifying operation, creating pipeline, and upgrading the new pipeline [25]. The main purpose of the modification operation is to serve the existing highly trusted pipelines, provide some new space points, and then realize the effective optimization of these pipeline attribute estimations. The created pipelines are used to form low-trust pipelines with loose boundaries in batches. Because space points can create new pipelines under their own actions or can be combined with existing low-trust pipelines, there are often many conflicts in low-trust pipelines. Upgrading new pipelines is mainly aimed at creating low-trust pipelines. First, it is evaluated under different conditions, and then, it is upgraded, namely, a new high-trust pipeline is generated.

3. Application of GPR in Urban Underground Pipeline Detection

3.1. Detection Results with Different Numbers of Pipelines. To explore the application effect of GPR in urban underground pipeline detection, it is necessary to preset the scanning density of the zig-shaped layout and the length of its scanning line. Regarding the environmental and operational parameters, it is necessary to set the location, number of underground pipelines, and boundary of credibility. For example, the detection result with only one tested pipeline is shown in Figure 6.

The strip connection in Figure 6 refers to the predefined tested pipeline, the dotted line represents the scanning line in detection, and the thicker line segment is the detected alarm point. Figures 6(a)–6(h) show the results of eight detection points. These results are obtained using the following methods: when a section of the scan line is added, the self-modified and filtered drawing algorithm of the underground pipeline goes through a run, and an updated 3D image is generated. The results of the detection experiment are arranged according to the increase in λ, and the number of alarm points continues to increase. When λ is set as 0, 0.1, 0.2, and 0.3, the underground pipelines whose errors are accepted are 0, 0, 2, and 5, respectively. When reaches 0.3, the self-correcting and filtering algorithm can still search out a highly trusted pipeline to track the predefined pipeline and show good tracking ability. On this basis, the detection results of the predefined pipeline are shown in Figure 7.

Each line segment in Figure 7 is consistent with that in Figure 6. Figure 7 shows that when λ is 0, 0.1, 0.2, and 0.3, the number of underground pipelines with accepted errors is 0, 1, 3, and 3, respectively. Comparing the two detection results with different numbers of pipelines, it can be seen that under the premise that the accuracy of the underground pipeline selected by the algorithm in this paper is higher, if the value of boundary condition N_0 is larger and the other conditions are consistent. In general, if the position error of the real space point satisfies $N(0, \sigma)$, then the range of boundary condition P_0 is $[2\sigma, 3\sigma]$, and the value of σ is negatively related to the upper limit of the detection algorithm. Since the strengthening constraint applied after MVP is MDA, for A_0, its value is much less than P_0.

3.2. Detection Results of Underground Pipeline Position in Different Highway Sections. To explore the accuracy of urban underground pipeline detection based on GPR, a series of experiments were carried out in three different highway sections, i.e., sections α, β, and γ. In section α, four survey lines were set as α-1, α-2, α-3, and α-4 to detect with GPR, and the relevant geometric dimension information of underground pipelines in this section after offset processing was obtained, as shown in Table 1.

According to Table 1, the top of the underground pipeline in the GPR image of line α-1 is located at 0.796 m depth of the horizontal position of the line, and the position of the underground pipeline is within the range of 0.419 m to 0.842 m of the horizontal position of the line. The burial depth and width of the underground pipeline are 1.379 m and 0.842 m, respectively. The relevant data of survey lines α-1, α-2, α-3, and α-4 are listed in Table 1. By comparing them with the actual positions of underground pipelines, it can be seen that the detection result error based on the electric sounding radar in the vertical direction is very small, within the range of 0.019 m to 0.199 m. In addition, the detection result error in the horizontal direction is even less than the former, with the detection error from 0.013 m to 0.139 m. This shows that the detection technology based on the electric sounding radar can show superior performance when detecting the α-section and meet accuracy and resolution requirements. The detection results of section β are shown in Table 2.

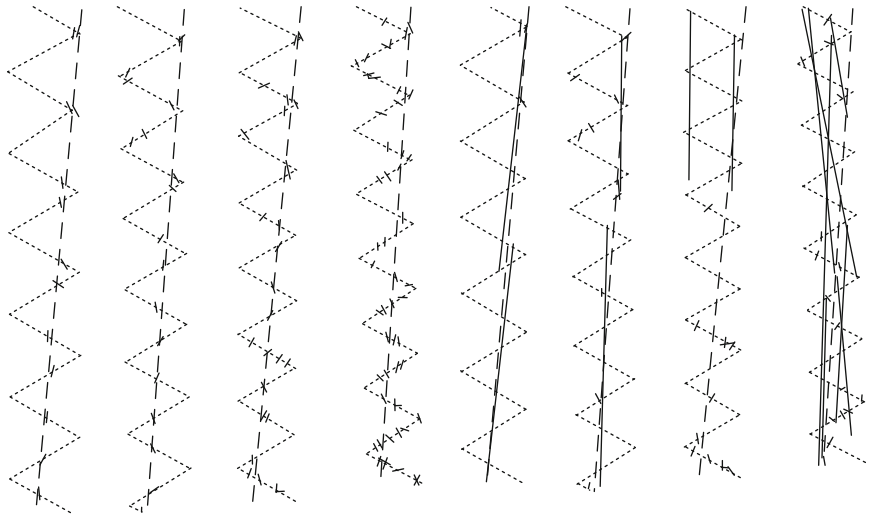

(a) $\lambda = 0$ (b) $\lambda = 0.1$ (c) $\lambda = 0.2$ (d) $\lambda = 0.3$ (e) $\lambda = 0$ (f) $\lambda = 0.1$ (g) $\lambda = 0.2$ (h) $\lambda = 0.3$

Figure 6: Detection results with only one tested pipeline.

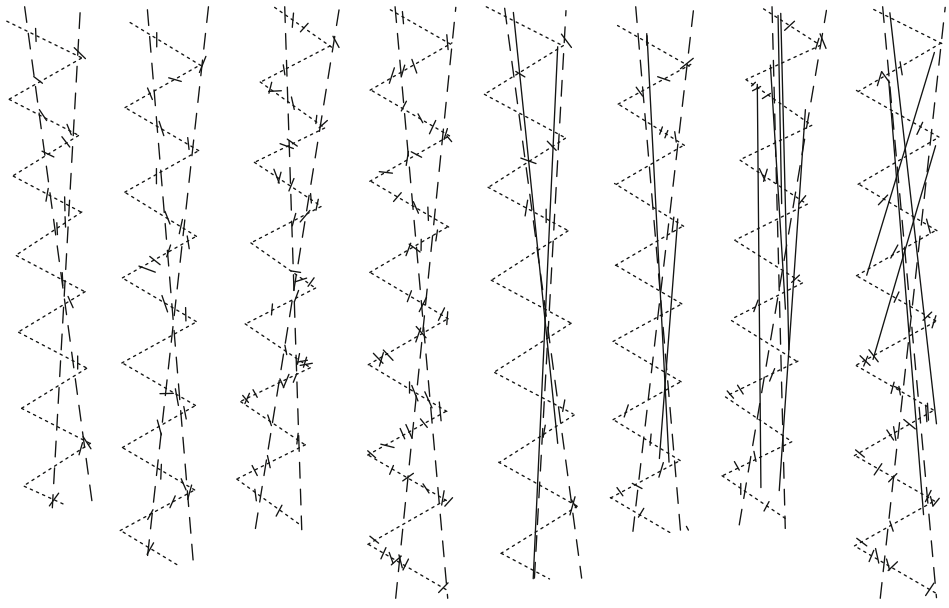

(a) $\lambda = 0$ (b) $\lambda = 0.1$ (c) $\lambda = 0.2$ (d) $\lambda = 0.3$ (e) $\lambda = 0$ (f) $\lambda = 0.1$ (g) $\lambda = 0.2$ (h) $\lambda = 0.3$

Figure 7: Detection results with two tested pipelines.

Table 1: Location of underground pipelines in section α.

Line number	α-1	α-2	α-3	α-4
The top of underground pipeline is at the horizontal position of the survey line (m)	0.796	4.473	2.577	0.945
The underground pipeline is located at the horizontal position of the survey line (m)	0.419 to 0.842	4.019 to 4.968	2.037 to 3.135	4.165 to 5.519
Buried depth of underground pipeline from ground (m)	1.379	1.069	1.387	1.037
Width of underground pipeline (m)	0.842	0.949	1.098	0.968

Table 2: Location of underground pipelines in section β.

Line number	β-1	β-2	β-3	β-4
The top of the underground pipeline is at the horizontal position of the survey line (m)	3.554	1.796	3.493	0.963
The underground pipeline is located at the horizontal position of the survey line (m)	2.732 to 3.930	1.472 to 2.446	3.022 to 3.895	0.569 to 1.450
Buried depth of underground pipeline from ground (m)	0.909	1.204	1.258	1.646
Underground pipeline width (m)	1.199	1.075	0.874	0.882

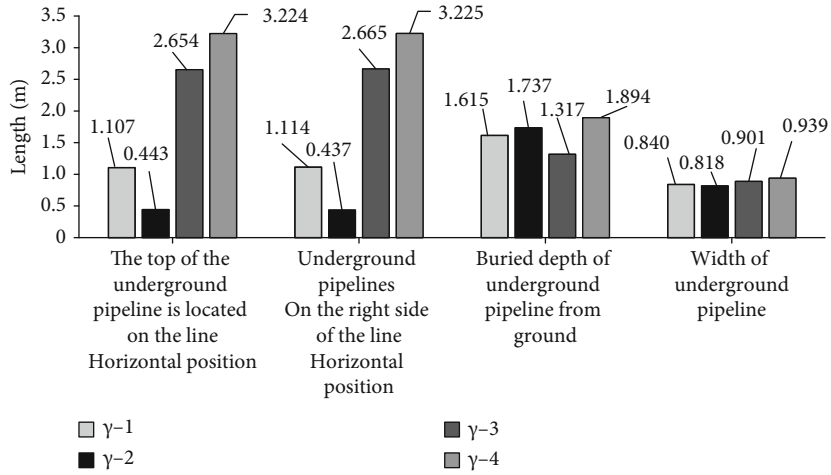

Figure 8: Location of underground pipelines in section γ.

After a series of operations, such as signal gain, filtering, and migration processing, the detection results of four different lines in section β can be obtained.

(1) The detection results of line β-1 show that the top of the underground pipeline is 3.554 m in the horizontal position, and its position is within the range of 2.732 m to 3.930 m from the horizontal position of the line. Moreover, the burial depth and width of the underground pipeline are 0.909 m and 1.199 m, respectively

(2) According to line β-2, the top of the underground pipeline is located at 1.796 m of the horizontal position of the line, and its position is located between 1.472 m and 2.446 m. Moreover, its buried depth and width are 1.204 m and 1.075 m, respectively

(3) Measurement of line β-3 indicates that the top of the underground pipeline is far from the horizontal position of its own line, reaching a depth of 3.493 m. The distance of the underground pipeline from the horizontal position of the line is between 3.022 m and 3.895 m. Moreover, its buried depth and width are 1.258 m and 0.874 m, respectively

(4) According to survey line β-4, the top of the underground pipeline is the closest to the horizontal position of the line, which is only 0.963 m. The distance between the underground pipeline and the horizontal position of the survey line is the shortest, which is between 0.569 m and 1.450 m. Moreover, the buried depth and width of the underground pipeline are 1.646 m and 0.882 m, respectively

Then, by comparing and analyzing the actual data and the above detection results in section β, it is found that the horizontal error between the two values ranges from 0.043 m to 0.201 m, while the vertical error is slightly less than the former, with a range of 0.020 m to 0.154 m. Such small errors show the high accuracy of urban underground pipeline detection based on GPR. The detection results of section γ are shown in Figure 8.

As shown in Figure 8, after offset processing, the detection result of line γ-1 shows that the top of the underground pipeline is 1.107 m away from the horizontal position of the line. The underground pipeline is located at 1.114 m of the horizontal position of line γ-1, and its buried depth and width are 1.615 m and 0.840 m, respectively. The detection results of line γ-2 show that the top of the underground pipeline is 0.443 m away from the horizontal position of the line, and the underground pipeline itself is 0.437 m away from the horizontal position of the line, with a buried depth of 1.737 m and width of 0.818 m. The detection results of line γ-3 show that the top of the underground pipeline is 2.654 m away from the horizontal position of the line. The underground pipeline itself is located at a depth of 2.665 m from the horizontal position of the line. The burial depth and width are 1.317 m and 0.901 m, respectively. The detection results of line γ-4 show that the top of the underground pipeline is 3.224 m away from the horizontal position of

the line. The burial depth and width of the underground pipeline are 1.894 m and 0.939 m, respectively, which are 3.225 m away from the horizontal position of the γ-4 survey line. Comparing the detection results with the actual data of the γ sections, it is found that the horizontal and vertical error ranges of the two are 0.014 m and 0.248 m and 0.095 m and 0.163 m, respectively. These minor errors confirm that the detection technology based on GPR has high detection accuracy and resolution.

4. Conclusions

With the continuous acceleration of China's urban modernization, earth shaking changes have taken place in the city. The normal operation of the city is closely related to the smoothness of underground pipelines. Urban underground pipelines cover many fields and contribute an important force to urban power operation, water supply, and drainage. To prevent the urban underground pipeline from aging, blocking, and other faults so that the urban underground pipeline can maintain its normal working state, regular maintenance is very important.

This subject experiment takes GPR as the research core and thoroughly analyzes the technical principle and layout design of GPR, as well as the underground pipeline drawing algorithm of self-correction and screening, and finally applies it to the detection technology of urban underground pipeline to compare and explore the detection effects under different conditions. The results show that under different numbers of verification pipelines, the Z-shaped layout can have a wider detection range and lower detection path cost. The detection results of underground pipeline positions in different sections also verify the detection performance of the detection technology α, Road section β, and Road section γ. In the three sections, the distance between the top of the underground pipeline and the horizontal position of the first survey line and the buried depth and width of the underground pipeline have small horizontal error and vertical error.

The previous underground pipeline detection technology can only perform the detection task in an environment with simple detection conditions and few obstacles, and the detection accuracy is low. It cannot ensure the effectiveness of the detection on the basis of expanding the detection range. Urban underground pipeline detection technology based on GPR can be well applied in different complex conditions and can show extremely superior detection performance, including high detection accuracy and high detection resolution.

Data Availability

The data reported in this article are available from the corresponding author upon request.

Conflicts of Interest

The authors declare no conflicts of interest,

Authors' Contributions

The manuscript has been approved by all authors for publication.

Acknowledgments

This research was supported by the National Natural Science Foundation of China (grant number 51678226), the Natural Science Foundation of Hunan Province (grant numbers 2021JJ50147 and 2021JJ30078), the Science and Technology Innovation Project of Yiyang City (grant numbers 2019YR02 and 2020YR02), and the Open Research Foundation of Hunan Provincial Key Laboratory of Key Technology on Hydropower Development (grant number PKLHD202005). The support is gratefully acknowledged.

References

[1] V. M. Smirnov, O. V. Yushkova, and V. N. Marchuk, "Using the subsurface soil sounding radar for investigating the structure and total electron content of the Martian ionosphere," *Cosmic Research*, vol. 56, no. 3, pp. 180–189, 2018.

[2] H. Wu, G. Y. Zhao, and S. W. Ma, "Failure behavior of horseshoe-shaped tunnel in hard rock under high stress: phenomenon and mechanisms," *Transactions of Nonferrous Metals Society of China*, vol. 32, no. 2, pp. 639–656, 2022.

[3] S. Li, Y. G. Zhang, M. Y. Cao, and Z. N. Wang, "Study on excavation sequence of pilot tunnels for a rectangular tunnel using numerical simulation and field monitoring method," *Rock Mechanics and Rock Engineering*, 2022.

[4] W. Zhong, J. Ouyang, D. X. Yang, X. J. Wang, Z. Q. Guo, and K. J. Hu, "*Effect of the in situ leaching solution of ion-absorbed rare earth on the mechanical behavior of basement rock*," *Journal of Rock Mechanics and Geotechnical Engineering*, 2021.

[5] G. S. Han, Y. Zhou, R. C. Liu, Q. Q. Tang, X. K. Wang, and L. B. Song, "*Influence of surface roughness on shear behaviors of rock joints under constant normal load and stiffness boundary conditions*," *Natural Hazards*, 2022.

[6] D. J. Pan, K. R. Hong, H. L. Fu, J. Zhou, N. Zhang, and G. Lu, "Influence characteristics and mechanism of fragmental size of broken coal mass on the injection regularity of silica sol grouting," *Construction and Building Materials*, vol. 269, p. 121251, 2021.

[7] W. Chu, D. M. Schroeder, and M. R. Siegfried, "Retrieval of englacial firn aquifer thickness from ice-penetrating radar sounding in Southeastern Greenland," *Geophysical Research Letters*, vol. 45, no. 21, pp. 11,770–11,778, 2018.

[8] A. E. Akpan, S. E. Ekwok, E. D. Ebong, A. M. George, and E. E. Okwueze, "Coupled geophysical characterization of shallow fluvio-clastic sediments in Agwagune, southeastern Nigeria," *Journal of African Earth Sciences*, vol. 143, pp. 67–78, 2018.

[9] K. Y. Sakharov, A. V. Sukhov, V. A. Turkin, O. V. Mikheev, and A. I. Aleshko, "Processing of signals and analysis of errors in measurements of electromagnetic parameters of radar-absorbing materials in the time domain," *Measurement Techniques*, vol. 60, no. 1, pp. 62–68, 2017.

[10] L. Bianco, K. Friedrich, J. M. Wilczak et al., "Assessing the accuracy of microwave radiometers and radio acoustic sounding systems for wind energy applications," *Atmospheric Measurement Techniques*, vol. 10, no. 5, pp. 1707–1721, 2016.

[11] X. Feng, Y. Yu, C. Liu, and M. Fehler, "Subsurface polarimetric migration imaging for full polarimetric ground-penetrating radar," *Geophysical Journal International*, vol. 202, no. 2, pp. 1324–1338, 2018.

[12] A. V. Zakharov, N. A. Eismont, V. M. Gotlib, V. M. Smirnov, O. V. Yushkova, and V. N. Marchuk, "Radiosounding in the planned mission to Phobos," *Solar System Research*, vol. 51, no. 5, pp. 386–399, 2017.

[13] Y. Harada, D. A. Gurnett, A. J. Kopf et al., "Dynamic response of the Martian ionosphere to an interplanetary shock: Mars Express and MAVEN observations," *Geophysical Research Letters*, vol. 44, no. 18, pp. 9116–9123, 2017.

[14] C. A. Bortolozo, O. Bokhonok, J. L. Porsani, F. A. Monteiro dos Santos, L. A. Diogo, and E. Slob, "Objective function analysis for electric soundings (VES), transient electromagnetic soundings (TEM) and joint inversion VES/TEM," *Journal of Applied Geophysics*, vol. 146, pp. 120–137, 2017.

[15] P. O. Barsukov and E. B. Fainberg, "Marine transient electromagnetic sounding of deep buried hydrocarbon reservoirs: principles, methodologies and limitations," *Geophysical Prospecting*, vol. 65, no. 3, pp. 840–858, 2017.

[16] T. S. Sreekanth, H. Varikoden, E. A. Resmi, and G. Mohan Kumar, "Classification and seasonal distribution of rain types based on surface and radar observations over a tropical coastal station," *Atmospheric Research*, vol. 218, pp. 90–98, 2019.

[17] D. Micheli, R. Pastore, A. Delfini et al., "Electromagnetic characterization of advanced nanostructured materials and multilayer design optimization for metrological and low radar observability applications," *Acta Astronautica*, vol. 134, no. 5, pp. 33–40, 2017.

[18] A. C. Ekwe, A. I. Opara, C. G. Okeugo et al., "Determination of aquifer parameters from geosounding data in parts of Afikpo Sub-basin, southeastern Nigeria," *Arabian Journal of Geosciences*, vol. 13, no. 4, pp. 1–15, 2020.

[19] D. Lee, W. Melek, and G. Shaker, "Investigation of wrapped effects on bow-tie antenna with and without resistive loading for pulsed radar applications," *Electronics Letters*, vol. 55, no. 1, pp. 7-8, 2019.

[20] J. X. Su, H. Yu, J. Y. Yu, Q. Guo, and Z. Li, "Tri-band radar cross-section reduction based on optimised multi-element phase cancellation," *IET Microwaves, Antennas & Propagation*, vol. 14, no. 15, pp. 2097–2101, 2020.

[21] D. Chrysostomou, A. Dimitriou, N. D. Kokkinos, and C. A. Charalambous, "Short-term electromagnetic interference on a buried gas pipeline caused by critical fault events of a wind park: a realistic case study," *IEEE Transactions on Industry Applications*, vol. 56, no. 2, pp. 1162–1170, 2020.

[22] S. R. Ravula, S. C. Narasimman, L. Wang, and A. Ukil, "Experimental validation of leak and water-ingression detection in low-pressure gas pipeline using pressure and flow measurements," *IEEE Sensors Journal*, vol. 17, no. 20, pp. 6734–6742, 2017.

[23] J. C. von Fischer, D. Cooley, S. Chamberlain et al., "Rapid, vehicle-based identification of location and magnitude of urban natural gas pipeline leaks," *Environmental Science & Technology*, vol. 51, no. 7, pp. 4091–4099, 2017.

[24] J. Li, Y. F. Li, Q. Bi et al., "Performance evaluation on fixed water-based firefighting system in suppressing large fire in urban tunnels," *Tunnelling and Underground Space Technology*, vol. 84, pp. 56–69, 2019.

[25] F. Li, W. Wang, S. Dubljevic, F. Khan, J. Xu, and J. Yi, "Analysis on accident-causing factors of urban buried gas pipeline network by combining DEMATEL, ISM and BN methods," *Journal of Loss Prevention in the Process Industries*, vol. 61, pp. 49–57, 2019.